RAA 2015 Vol. **15** No. **9**, 1537–1546 doi: 10.1088/1674–4527/15/9/010
http://www.raa-journal.org *http://www.iop.org/journals/raa*

Research in Astronomy and Astrophysics

Comparison between the eruptive X2.2 flare on 2011 February 15 and confined X3.1 flare on 2014 October 24

Ju Jing[1,2], Yan Xu[1,2], Jeongwoo Lee[1,3], Nariaki V. Nitta[4], Chang Liu[1,2], Sung-Hong Park[5], Thomas Wiegelmann[6] and Haimin Wang[1,2]

[1] Center for Solar-Terrestrial Research, New Jersey Institute of Technology, Newark, NJ 07102-1982, USA; *ju.jing@njit.edu*
[2] Big Bear Solar Observatory, Big Bear City, CA 92314, USA
[3] Astronomy Program, Department of Physics and Astronomy, Seoul National University, Seoul 151-747, Korea
[4] Lockheed Martin Solar and Astrophysics Laboratory, Palo Alto, CA 94304, USA
[5] Institute for Astronomy, Astrophysics, Space Applications and Remote Sensing (IAASARS), National Observatory of Athens, Penteli 15236, Greece
[6] Max-Planck-Institut fuer Sonnensystemforschung, Justus-von-Liebig-Weg 3, 37077 Goettingen, Germany

Received 2015 May 15; accepted 2015 June 30

Abstract We compare two contrasting X-class flares in terms of magnetic free energy, relative magnetic helicity and decay index of the active regions (ARs) in which they occurred. The events in question are the eruptive X2.2 flare from AR 11158 accompanied by a halo coronal mass ejection (CME) and the confined X3.1 flare from AR 12192 with no associated CME. These two flares exhibit similar behavior of free magnetic energy and helicity buildup for a few days preceding them. A major difference between the two flares is found to lie in the time-dependent change of magnetic helicity of the ARs that hosted them. AR 11158 shows a significant decrease in magnetic helicity starting $\sim$4 hours prior to the flare, but no apparent decrease in helicity is observed in AR 12192. By examining the magnetic helicity injection rates in terms of sign, we confirmed that the drastic decrease in magnetic helicity before the eruptive X2.2 flare was not caused by the injection of reversed helicity through the photosphere but rather the CME-related change in the coronal magnetic field. Another major difference we find is that AR 11158 had a significantly larger decay index and therefore weaker overlying field than AR 12192. These results suggest that the coronal magnetic helicity and the decay index of the overlying field can provide a clue about the occurrence of CMEs.

Key words: Sun: magnetic topology — Sun: evolution — Sun: flares — Sun: coronal mass ejections (CMEs)

1 INTRODUCTION

A solar flare, especially a large two-ribbon flare, is often associated with a coronal mass ejection (CME). However, there are also many cases to the contrary. In this paper we will use the terms "eruptive" and "confined" to describe flares with and without CMEs, respectively.

Although there is no doubt that the magnetic field is involved in determining whether a flare is eruptive or confined, full understanding still remains elusive. Two factors that we can think of are magnetic helicity and free energy budgets in active regions (ARs). As suggested by some magnetohydrodynamic (MHD) simulations, the accumulation of helicity may lead to an instability that can be alleviated when the Sun ejects helicity via launching a CME (Low 1994, 1997; Amari et al. 2003a,b; Jacobs et al. 2006). This idea has been supported by many observations (e.g., LaBonte et al. 2007; Tziotziou et al. 2012). For instance, Nindos & Andrews (2004) extrapolated linear force-free coronal magnetic fields of ARs, with which the twist parameter α ($\nabla \times \boldsymbol{B} = \alpha \boldsymbol{B}$) of each AR was computed as a proxy of magnetic helicity. Based on a large sample, they found that the average value of pre-flare α in ARs producing eruptive flares is significantly larger than that in ARs producing confined flares. A more recent statistical study by Tziotziou et al. (2012) showed that ARs with eruptive flares are well segregated from ARs with confined flares in both helicity and free energy. They estimated the thresholds for ARs to produce eruptive flares, which are $\sim 2 \times 10^{42}$ Mx^2 and $\sim 4 \times 10^{31}$ erg for relative helicity and free energy, respectively. In addition, the MHD model by Kusano et al. (2004) suggests that the eruption is triggered by the injection of reversed helicity into a filament channel, which is evidenced by some observations (Vemareddy et al. 2012; Park et al. 2012). There are, however, different views that CMEs can occur independently of helicity (e.g., Phillips et al. 2005; Zuccarello et al. 2009). A clue comes from the study of the torus instability of a magnetic flux rope. The MHD simulation shows that a sufficiently rapid decay of the external field with height above the flux rope allows development of a CME (Török & Kliem 2005; Kliem & Török 2006; Török & Kliem 2007). In this respect, the gradient in the external field with height, referred to as "decay index," can be used to estimate how much the eruption is suppressed by the external field. The critical threshold beyond which an eruption is more likely to occur typically falls into a range of 1.1–2.0 (Bateman 1978; Fan & Gibson 2007; Schrijver et al. 2008; Démoulin & Aulanier 2010; Xu et al. 2012).

In this paper, we present observations of two particularly well-observed X-class flares, the eruptive X2.2 flare of AR 11158 which leads to a pronounced halo CME and the confined X3.1 flare of AR 12192 which is not associated with a CME. It is worth mentioning that the "CME-poor" property of AR 12192 has attracted a great deal of attention lately (e.g., Thalmann et al. 2015), and its possible magnetic cause, in brief "weaker non-potentiality and stronger overlying field," is discussed by Sun et al. (2015). We complement those works by studying the evolution of the magnetic field beyond the flare periods, which should be needed for a complete assessment of the role of magnetic complexity in producing CMEs. Specifically, in each case of the flares, we investigate the evolution of free magnetic energy $E_{\rm free}$, relative magnetic helicity $H_{\rm r}$ and decay index n of the hosting ARs over days during their disk passage. In Section 2, we briefly introduce a set of equations that are used to estimate the above-mentioned magnetic parameters. The observations and analysis results are presented and summarized in Section 3 and Section 4, respectively.

2 THE MAGNETIC PARAMETERS

Magnetic helicity is a topological measure of magnetic field structure, and also a key quantity in various MHD models (see Démoulin 2007 for a review). For decades, helicity mostly remained a theoretical concept in MHD models due to uncertainties related to the coronal magnetic field. Thanks to the recent development of the nonlinear force-free (NLFF) field extrapolation technique (e.g., Wiegelmann & Inhester 2010; Wiegelmann et al. 2012; Tadesse et al. 2013), helicity contained within a three-dimensional (3D) volume from photosphere to corona can be quantitatively derived

from observations (Park et al. 2010; Jing et al. 2012). Note that for the solar corona, only relative magnetic helicity $H_{\rm r}$ (relative to a reference potential field in the present study) can be estimated, and for simplicity, the term "helicity" will be used for relative magnetic helicity throughout this paper. Here $H_{\rm r}$ is defined as (Berger & Field 1984; Finn & Antonsen 1984)

$$H_r = \int_V (\boldsymbol{A}_{\rm nlff} + \boldsymbol{A}_{\rm p}) \cdot (\boldsymbol{B}_{\rm nlff} - \boldsymbol{B}_{\rm p})\, dV, \tag{1}$$

where V is the 3D volume of the computational domain from photosphere to corona, $\boldsymbol{B}$ is the vector representation of the magnetic field, $\boldsymbol{A}$ is the vector potential of $\boldsymbol{B}$ ($\boldsymbol{B} = \nabla \times \boldsymbol{A}$), and the subscripts 'nlff' and 'p' represent the NLFF field and the potential field, respectively. Following DeVore (2000) and Fan (2009), we used the Coulomb gauge for vector potentials ($\nabla \cdot \boldsymbol{A} = 0$) which also have a vanishing normal component at the surface. In this case, the potential helicity integral vanishes and $H_{\rm r}$ reduces to simply $H_{\rm r} = \int_V \boldsymbol{A}_{\rm nlff} \cdot \boldsymbol{B}_{\rm nlff}\, dV$ (DeVore 2000; Fan 2009).

Free magnetic energy $E_{\rm free}$ is defined as

$$E_{\rm free} = E_{\rm nlff} - E_{\rm p} = \int_V \frac{\boldsymbol{B}^2_{\rm nlff}}{8\pi} dV - \int \frac{\boldsymbol{B}^2_{\rm p}}{8\pi}\, dV. \tag{2}$$

It quantifies the energy deviation of the magnetic field from its potential state, and is regarded as the upper limit of energy that is available to power flares/CMEs.

Decay index n is defined as (Kliem & Török 2006)

$$n = -\frac{\partial \log(B_{\rm ex})}{\partial \log(h)}, \tag{3}$$

where $B_{\rm ex}$ is the strength of the horizontal component of the external field and h is the height above the solar surface. Instead of an NLFF field, the potential field is often used to estimate the decay index of the external field (e.g., Liu 2008; Xu et al. 2012), as the external field confining the erupting core field usually lies in a height range of a few tens to about a hundred Mm where the coronal field approaches a potential configuration (Jing et al. 2008).

3 OBSERVATIONS AND RESULTS

The eruptive X2.2 flare occurred in AR 11158 on 2011 February 15, and was first observed by *GOES* soft X-ray (SXR) emission at 01:44 UT, with a maximum flux at 01:56 UT. At the time of the flare, AR 11158 was located at (S20°, W13°) and classified as $\beta\gamma$. On the other hand, the confined X3.1 flare occurred in AR 12192 on 2014 October 24. The times when the SXR flux started to increase and reach its maximum were 21:07 UT and 21:41 UT, respectively. At the time of the flare, AR 12192 was located at (S13°, W16°) and reached the rank of the largest sunspot complex in the current solar cycle 24, in a $\beta\gamma\delta$ configuration. The entire course of two flares and the evolution of two hosting ARs were observed by Atmospheric Imaging Assembly (AIA; Lemen et al. 2012) and Helioseismic and Magnetic Imager (HMI; Schou et a. 2012) on board the *Solar Dynamics Observatory* (*SDO*; Pesnell et al. 2012). Selective AIA 171 Å images in the early phase of the flares and the corresponding HMI line-of-sight (LOS) magnetograms are shown in Figure 1. Apparently, AR 11158 was comprised of two bipolar regions side by side. The X2.2 flare took place in the core of this double bipolar environment with two flare ribbons straddling the strong-gradient, highly-sheared polarity inversion line (PIL) between the inner spot clusters (Schrijver et al. 2011). By comparison, the giant AR 12192 seems to have a simpler configuration than AR 11158. The primary sunspot clusters with opposite polarities drifted away to leave a weak field region between them, and the X3.1 flare initiated in this region and extended southward in time.

To extrapolate the 3D NLFF and potential field of the ARs we use the latest version of the HMI photospheric vector magnetograms in Space weather HMI Active Region Patches (SHARP)

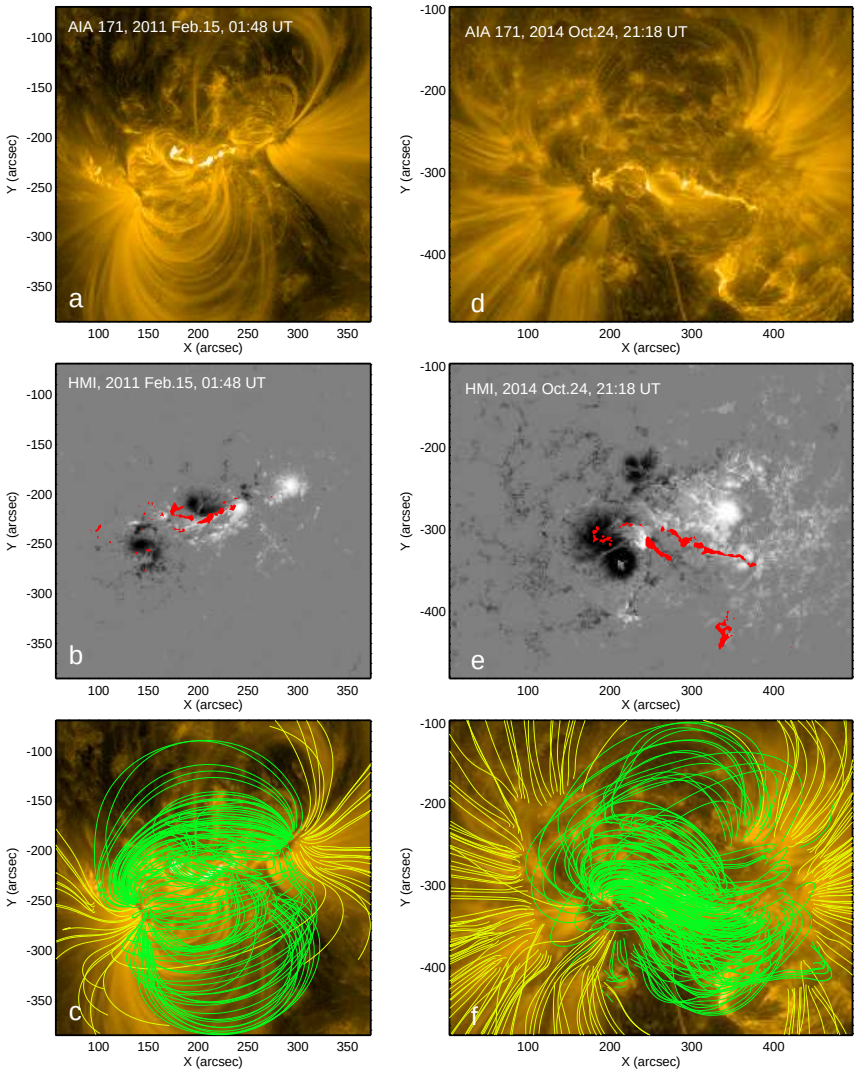

Fig. 1 The X2.2 flare and its hosting AR 11158 (*left column*) and the X3.1 flare and its hosting AR 12192 (*right column*). (a)–(b): An AIA 171 Å image and an HMI line-of-sight magnetogram taken in the early phase of the X2.2 flare. The red contours indicate the locations of the flare ribbons as seen in the AIA 171 Å image. (c): Sample NLFF field lines overlaid on the AIA 171 Å image. The closed field lines are colored green, and those field lines reaching the lateral/top boundaries of the computational domain are colored yellow. (d)–(f): same as (a)–(c), but for the X3.1 flare of AR 12192.

(Turmon et al. 2010) as the boundary conditions. The data series span the time from 2011 February 12 to 15 for the X2.2 flare of AR 11158, and from 2014 October 19 to 27 for the X3.1 flare of AR 12192. Since the tasks of NLFF field extrapolations and H_r calculations are computationally demanding, we generally use a time cadence of 1-hour, except for the periods around the flares over which the full 12-min cadence is used. With this analysis, each vector magnetogram was disambiguated to determine the azimuth angle in the full range of 0° to 360° using the minimum

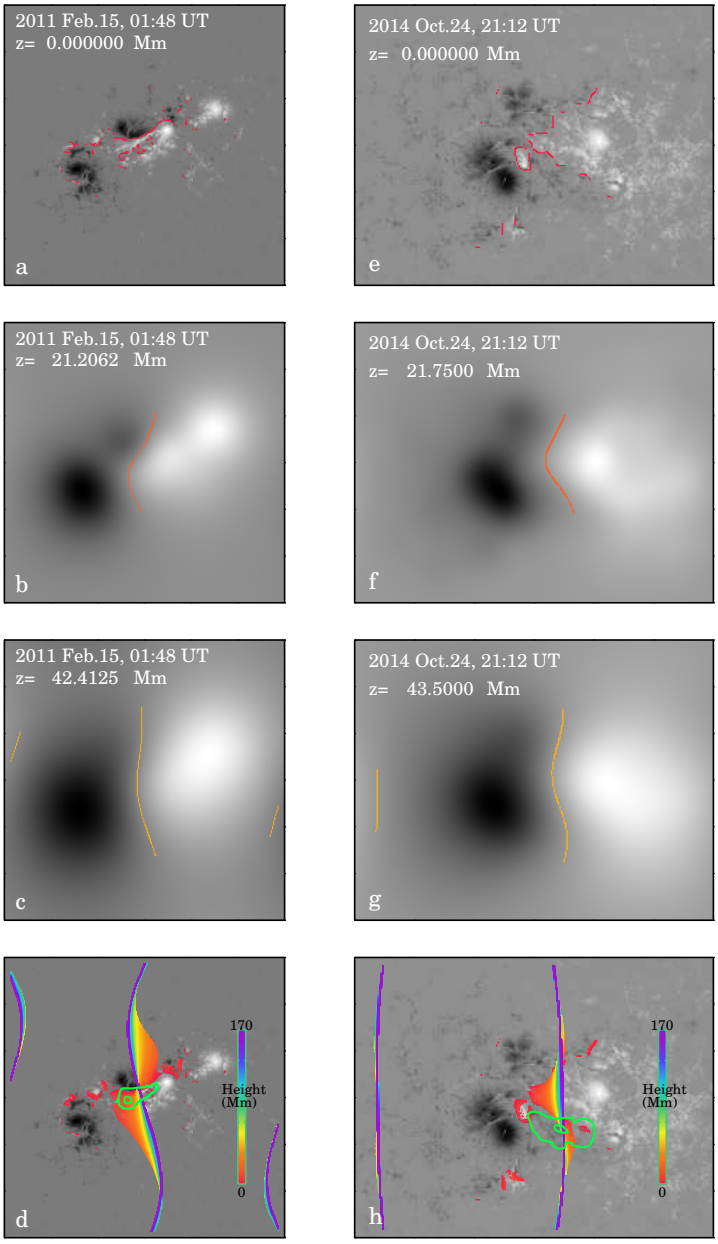

Fig. 2 The magnetic PILs evolving with height of AR 11158 (*left column*) and those of AR 12192 (*right column*). (a)–(c): The potential magnetic field (*grey scale*) at three selected heights, with the corresponding magnetic PILs (*colored*) superimposed. (d): The PILs from photosphere to corona are plotted together with the color code that is shown in the inset. (e)–(h): same as (a)–(d), but for AR 12192. Green contours in the bottom panels mark the *RHESSI* HXR intensity integrated in the time intervals of 01:55:00 – 01:56:00 UT (panel d, AR 11158) and 21:15:30 – 21:16:30 UT (panel h, AR 12192) in the 25–50 keV energy range.

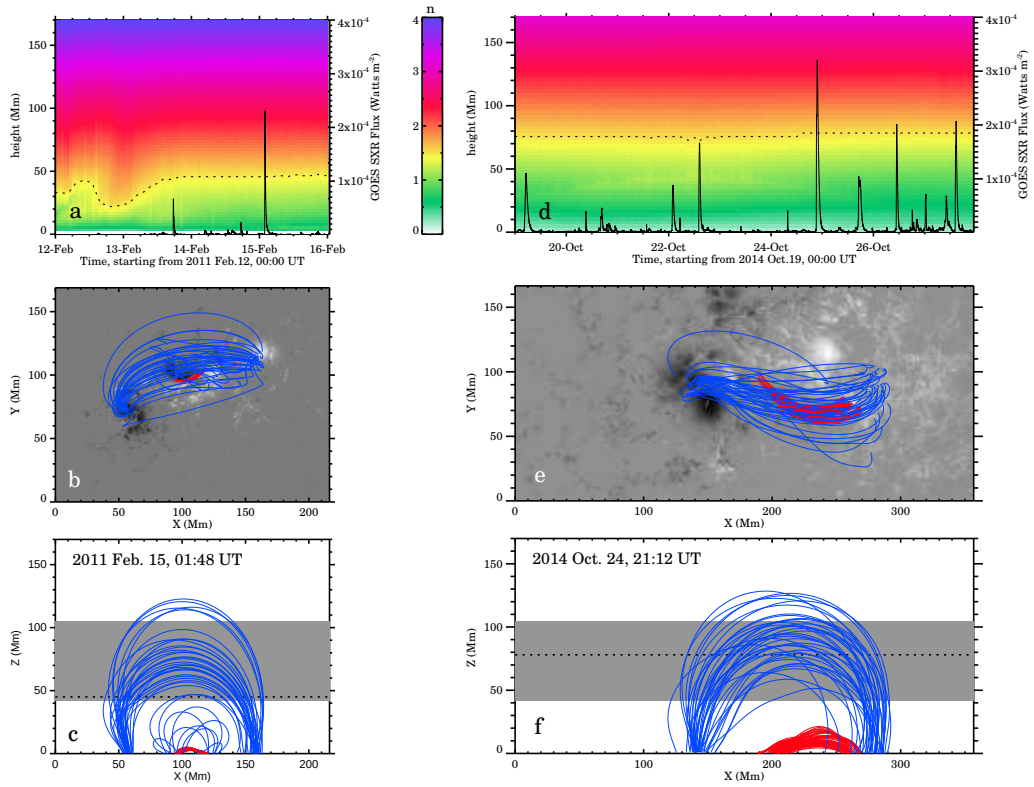

Fig. 3 Decay index n and magnetic configuration of AR 11158 (*left column*) and that of AR 12192 (*right column*). (a): The time-height diagram of n, with the *GOES* SXR (*black-solid*) light curve being overlaid. The dashed curve is the critical height where n reaches 1.5. (b): A bundle of twisted field lines (*red*) which is suggestive of a flux rope configuration, and the overlying field lines (*blue*), both of which are from the NLFF field extrapolation of 2011 Feb. 15, 01:48 UT. (c): The projection of the same flux rope and external field on the x-z plane. The grey area indicates a height range of 42−105 Mm, and the dashed line signifies the critical height at this moment. (d)–(f): same as (a)–(c), but for AR 12192. The magnetic configurations shown in (e) and (f) are from the NLFF field extrapolation of 2014 Oct. 24, 21:12 UT.

energy method (Metcalf 1994; Leka et al. 2009), and was re-mapped onto heliographic coordinates using the Lambert Cylindrical Equal-Area projection method (Calabretta & Greisen 2002). We pre-processed the data towards the force-free conditions (Wiegelmann et al. 2006), and used the latest version of the weighted optimization method of Wiegelmann & Inhester (2010), which is optimized for HMI data (Wiegelmann et al. 2012), to extrapolate the NLFF fields. For AR 11158, the extrapolation was performed within a computational domain of 256×256×200 pixels, corresponding to ∼217×217×170 Mm^3. For AR 12192, the extrapolation was performed within a computational domain of 256×200×200 pixels, corresponding to a larger volume of ∼371×290×290 Mm^3. The comparison between some extrapolated NLFF field lines and the observed coronal loops seen in the 171 Å channel shows an overall similarity between the NLFF field model and the observations (Fig. 1(c) and 1(f)).

Since the horizontal field above the PIL provides the primary constraining force that inhibits the eruption, decay index n of the external field is usually computed over a slim region along the

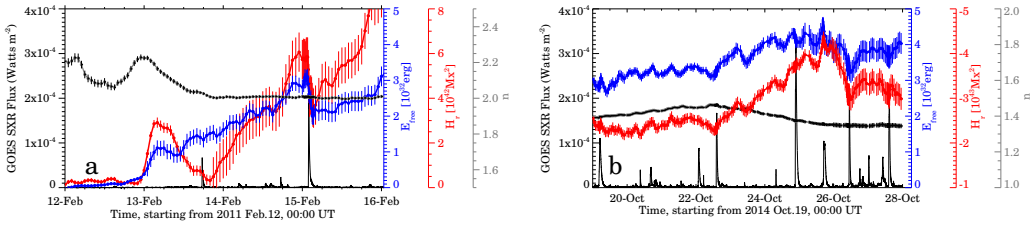

Fig. 4 Temporal variation of helicity $H_{\rm r}$ (*red*), free magnetic energy $E_{\rm free}$ (*blue*), decay index n (*grey*), and *GOES* soft X-ray (1 – 8 Å) flux (*black*) of AR 11158 (a) and AR 12192 (b).

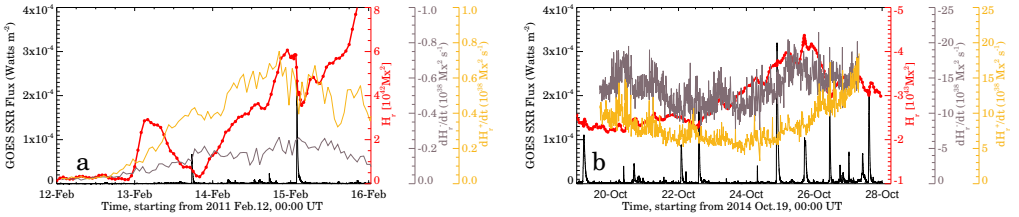

Fig. 5 Temporal variation of helicity $H_{\rm r}$ (*red*), *GOES* soft X-ray (1 – 8 Å) flux (*black*), negative helicity flux $\frac{dH_r^-}{dt}$ (*grey*) and positive helicity flux $\frac{dH_r^+}{dt}$ (*yellow*) through the photosphere of AR 11158 (a) and AR 12192 (b).

major PIL (e.g., Sun et al. 2015). However, the PIL observed at the photosphere may noticeably change its position and orientation with increasing height, and hence the regions selected based on the photospheric field may not be able to appropriately represent the external field in the corona. As an example, Figure 2 shows the PILs associated with the two ARs, which are derived from the potential field extrapolation, changing with height at two selected times. For AR 11158 (left column), the PIL in the photosphere is in the east-west orientation on a large scale, and rotates counterclockwise with height. For AR 12192 (right column), the V-shaped PIL in the photosphere becomes straight with height. In both cases, the orientation appears to change most obviously below $\sim$40 Mm and approximately remains stable some 40 to 100 Mm above the surface.

In this study, n is calculated as the gradient of the horizontal potential field with respect to height, averaged over the major PIL at each specific height. Note that position, orientation and length of a PIL vary with height as shown in Figure 2(d) and 2(h). The top panels of Figure 3 show the time-height diagrams of n for the two ARs. The dashed curves indicate the critical height where n reaches 1.5 so that torus instability may occur (Kliem & Török 2006). The critical height of the eruptive flare of AR 11158 is 45 Mm, lower than 78 Mm found in the confined flare of AR 12192. This readily indicates that the external field of the eruptive flare decays more rapidly than that of the confined flare. Figure 3(b)−3(c) and 3(e)−3(f) shows the flux rope and the overlying external field of two ARs, from the NLFF field extrapolation at the onset of the flares. The grey area marks a height range of 42−105 Mm that was often used in many previous computations of n (e.g., Liu 2008; Liu et al. 2010; Xu et al. 2012), as the CME activation usually occurs in this height zone (see Liu 2008, and references therein).

Another interesting phenomenon found here is that the PIL seemingly rotates with ascending height about a certain point (or an axis if we take the variation of height into account). We check the spatial correlation between this pivot point and the site of non-thermal energy release.

Figure 2(d) and 2(h) shows the *RHESSI* hard X-ray (HXR) sources (green contours) at the flare onsets and the PILs from photosphere to corona which are plotted together (colored curves). Evidently, the HXR source appears in close proximity to the pivot point of the PIL.

Figure 4 shows the evolution of $E_{\rm free}$, $H_{\rm r}$ and n in the two ARs. Here n is the field gradient with height (as shown in Fig. 3(a) and 3(d)) averaged in the height range of 42−105 Mm. In both cases, we find a gradual build-up of pre-flare helicity and energy and a decrease in energy from before to after the flares. Although they show such similarities on a qualitative basis, there are many significant quantitative differences. First, both ARs are located in the southern hemisphere, but they exhibit opposite signs of helicity. AR 11158 shows positive helicity, consistent with the hemispheric helicity rule (Pevtsov & Balasubramaniam 2003); whereas AR 12192 shows negative helicity which is not a common feature in the southern hemisphere. Second, two ARs are distinct from each other in terms of the strength of the overlying field. The time profile for n of AR 11158 varies between 2.0 and 2.2 during the early development stage of the AR. Then n stays at a value of 2.0 for $\sim$24 h prior to the X2.2 flare and remains steady towards the end of observation. This value is in general above the critical thresholds, 1.1−2.0, found in earlier studies (Xu et al. 2012 and reference therein). On the other hand, n of AR 12192 changes according to a clear pattern. It first increases gradually over an 84-hour period from 1.4 to 1.46, and then decreases gradually to 1.35 over time. This decreasing phase, which may help to stabilize the configuration, occurs $\sim$54 h prior to the X3.1 flare. The value of n around the time of the X3.1 flare is $\sim$1.37, which is below the critical threshold of 1.9 found by Fan & Gibson (2007) and below 1.5 found by Török & Kliem (2007) and Aulanier et al. (2010). Third, although the amount of $H_{\rm r}$ contained in AR 12192 is one order of magnitude larger than that in AR 11158, the former exhibits little, if any, decrease associated with its X3.1 flare. By comparison, the time profile of $H_{\rm r}$ of AR 11158 shows an apparent decrease, beginning $\sim$4 h prior to the X2.2 flare and lasting till the very end of the flare. AR 11158 loses about 45% of $H_{\rm r}$ during this decreasing phase.

Note that a significant decrease in helicity is also found well before the eruptive M6.6 flare of AR 11158 on 2011 February 13 and the confined X2.0 flare of AR 12192 on 2014 October 26. The decrease in coronal helicity could result either from the shedding of twisted flux ropes by the CME into interplanetary space or from injection of reversed helicity through the photosphere. We thus investigate the evolution of the magnetic helicity injection in terms of sign.

Figure 5 shows the injection rates of the positive and negative magnetic helicities (yellow and grey curves, respectively) of two ARs, calculated with HMI Active Region Patches (HARPs) magnetogram data using Pariat et al.'s (2005) method. AR 11158 was dominated by the positive helicity, and there was no considerable injection of the negative helicity into it prior to the eruptive flares. This implies that the decrease of coronal helicity (red curve) is more likely to be associated with the change of coronal magnetic field due to the CME. On the other hand, we can see that on 2014 October 26 there was a significant injection of positive helicity into AR 12192 in which the negative helicity dominated. We consider that such an injection of reversed helicity underlies the decrease of coronal helicity prior to the confined X2.0 flare.

4 SUMMARY AND INTERPRETATION

The present study compares two contrasting X-class flares in terms of the nonpotentiality of the hosting ARs (AR 12192 and AR 11158) and the constraining effect of the overlying external field. In a similar work, Sun et al. (2015) evaluated the instantaneous magnetic conditions of the CME-poor AR 12192 and two other CME-productive ARs including AR 11158, and attributed the CME-poor activity of AR 12192 to its weak non-potentiality and strong overlying field. Our study has gone a step further by studying the magnetic field evolution over days when the ARs were present. The instantaneous pre-flare energy and helicity budgets found for both eruptive and confined flares are well above the thresholds required for eruptive flares as set by Tziotziou et al. (2012).

A clear distinction between the two cases is their overlying field. Compared to the eruptive flare, the confined flare occurred in an AR with a higher critical height and a stronger overlying field. Such an overlying field may help to stabilize the flux rope and make it more difficult to erupt. Sun et al. (2015) presented a similar result, but in this study variations of the decay index with time and height are investigated in more detail.

We also note that a difference between the two flares lies in the temporal variation of the magnetic field. For the eruptive X2.2 flare, a drastic decrease in the magnitudes of the AR's helicity occurred well before and lasted throughout the flare, but no apparent decrease in helicity is observed for the confined X3.1 flare. The time profiles of helicity injection rate in terms of sign rule out the possibility that the drastic decrease in helicity before the eruptive X2.2 flare was caused by the injection of reversed helicity through the photosphere. Therefore, our result may suggest that the change of magnetic field due to the CME had probably been going on well before the flare-associated magnetic reconnection occurred. It is worth mentioning that, although an eruptive flare tends to be preceded by a decrease in helicity, not all the decrease in helicity is followed by an eruptive flare. For instance, a drastic decrease in helicity of AR 12192 starting on October 25 $\sim$21:00 UT is followed by a confined X2.0 flare. In this case, a significant injection of reversed helicity is the cause for the helicity decrease.

In addition, comparison of our magnetic field model with the *RHESSI* maps reveals that the non-thermal HXR source is apparently closely related to the change of PIL with height. This may imply a direct connection between the coronal magnetic configuration and the site of non-thermal energy release. Physical interpretation of this finding has yet to be made. At present we tentatively interpret this result as indicating that the change of PIL orientation from the photosphere to the corona can provide a clue to the likelihood of a coronal magnetic configuration being unstable. We intend to investigate this phenomenon and its underlying physics in the future.

Acknowledgements J. J., Y. X., C. L. and H. W. were supported by NASA under grants NNX11AQ55G, NNX13AG13G and NNX13AF76G, and NSF under grants AGS-1153226, AGS-1153424, AGS-1250374, AGS-1348513 and AGS- 1408703. J.L. was supported by the Brainpool program 2014 of KOFST and the BK21 Plus Program (21A20131111123) funded by the Ministry of Education (MOE, Korea) and National Research Foundation of Korea (NRF). N.V.N. was supported by the NSF grant AGS-1259549. S.P. was supported by the project "SOLAR-4068" under the "ARISTEIA II" Action and by the U.S. Air Force Research Laboratory under grant FA 2386-14-1-4078. T. W. was supported by DLR-grant 50 OC 0501. We thank the NASA/*SDO* team for providing the photospheric magnetograms and UV/EUV filtergrams.

References

Amari, T., Luciani, J. F., Aly, J. J., Mikic, Z., & Linker, J. 2003a, ApJ, 585, 1073
Amari, T., Luciani, J. F., Aly, J. J., Mikic, Z., & Linker, J. 2003b, ApJ, 595, 1231
Aulanier, G., Török, T., Démoulin, P., & DeLuca, E. E. 2010, ApJ, 708, 314
Bateman, G. 1978, MHD Instabilities (Cambridge, Mass: MIT Press)
Berger, M. A., & Field, G. B. 1984, Journal of Fluid Mechanics, 147, 133
Calabretta, M. R., & Greisen, E. W. 2002, A&A, 395, 1077
Démoulin, P. 2007, Advances in Space Research, 39, 1674
Démoulin, P., & Aulanier, G. 2010, ApJ, 718, 1388
DeVore, C. R. 2000, ApJ, 539, 944
Fan, Y., & Gibson, S. E. 2007, ApJ, 668, 1232
Fan, Y. 2009, ApJ, 697, 1529
Finn, J., & Antonsen, T. M., Jr. 1984, Comments Plasma Phys. Controlled Fusion, 9, 111
Jacobs, C., Poedts, S., & van der Holst, B. 2006, A&A, 450, 793

Jing, J., Wiegelmann, T., Suematsu, Y., Kubo, M., & Wang, H. 2008, ApJ, 676, L81
Jing, J., Park, S.-H., Liu, C., et al. 2012, ApJ, 752, L9
Kliem, B., & Török, T. 2006, Physical Review Letters, 96, 255002
Kusano, K., Maeshiro, T., Yokoyama, T., & Sakurai, T. 2004, ApJ, 610, 537
LaBonte, B. J., Georgoulis, M. K., & Rust, D. M. 2007, ApJ, 671, 955
Leka, K. D., Barnes, G., Crouch, A. D., et al. 2009, Sol. Phys., 260, 83
Lemen, J. R., Title, A. M., Akin, D. J., et al. 2012, Sol. Phys., 275, 17
Liu, C., Lee, J., Jing, J., et al. 2010, ApJ, 721, L193
Liu, Y. 2008, ApJ, 679, L151
Low, B. C. 1994, in ESA Special Publication, 373, Solar Dynamic Phenomena and Solar Wind Consequences, the Third SOHO Workshop, ed. J. J. Hunt, 123
Low, B. C. 1997, in Coronal Mass Ejections, Geophys. Monogr. Ser., 99, The Role of Coronal Mass Ejections in Solar Activity, eds. N. Crooker, J. Joselyn, & J. Feynman (Washington DC: American Geophysical Press), 39
Metcalf, T. R. 1994, Sol. Phys., 155, 235
Nindos, A., & Andrews, M. D. 2004, ApJ, 616, L175
Park, S.-H., Chae, J., Jing, J., Tan, C., & Wang, H. 2010, ApJ, 720, 1102
Park, S.-H., Cho, K.-S., Bong, S.-C., et al. 2012, ApJ, 750, 48
Pesnell, W. D., Thompson, B. J., & Chamberlin, P. C. 2012, Sol. Phys., 275, 3
Pevtsov, A. A., & Balasubramaniam, K. S. 2003, Advances in Space Research, 32, 1867
Phillips, A. D., MacNeice, P. J., & Antiochos, S. K. 2005, ApJ, 624, L129
Schrijver, C. J., Elmore, C., Kliem, B., Török, T., & Title, A. M. 2008, ApJ, 674, 586
Schrijver, C. J., Aulanier, G., Title, A. M., Pariat, E., & Delannée, C. 2011, ApJ, 738, 167
Sun, X., Bobra, M. G., Hoeksema, J. T., et al. 2015, ApJ, 804, L28
Tadesse, T., Wiegelmann, T., Inhester, B., et al. 2013, A&A, 550, A14
Thalmann, J. K., Su, Y., Temmer, M., & Veronig, A. M. 2015, ApJ, 801, L23
Török, T., & Kliem, B. 2005, ApJ, 630, L97
Török, T., & Kliem, B. 2007, Astronomische Nachrichten, 328, 743
Turmon, M., Jones, H. P., Malanushenko, O. V., & Pap, J. M. 2010, Sol. Phys., 262, 277
Tziotziou, K., Georgoulis, M. K., & Raouafi, N.-E. 2012, ApJ, 759, L4
Vemareddy, P., Ambastha, A., Maurya, R. A., & Chae, J. 2012, ApJ, 761, 86
Wiegelmann, T., Inhester, B., & Sakurai, T. 2006, Sol. Phys., 233, 215
Wiegelmann, T., & Inhester, B. 2010, A&A, 516, A107
Wiegelmann, T., Thalmann, J. K., Inhester, B., et al. 2012, Sol. Phys., 281, 37
Xu, Y., Liu, C., Jing, J., & Wang, H. 2012, ApJ, 761, 52
Zuccarello, F. P., Jacobs, C., Soenen, A., et al. 2009, A&A, 507, 441